ChemComm

Accepted Manuscript

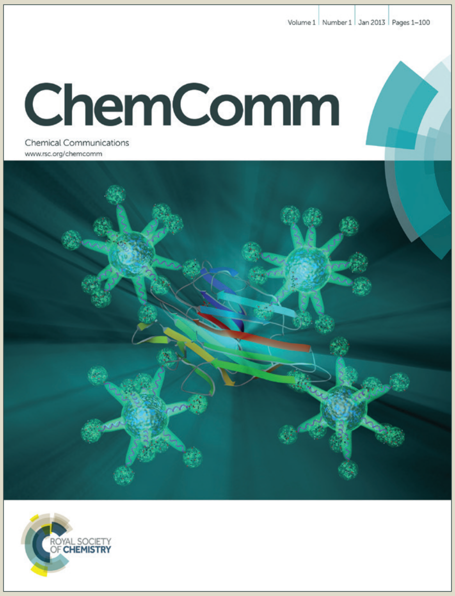

ROYAL SOCIETY OF CHEMISTRY

www.rsc.org/chemcomm

ChemComm RSCPublishing

COMMUNICATION

Cite this: DOI: 10.1039/x0xx00000x

Received 00th January 2015,
Accepted 00th January 2015

DOI: 10.1039/x0xx00000x

www.rsc.org/

Rational Design of Octahedron and Nanowire CeO_2@MnO_2 Core-Shell Heterostructures with Outstanding Rate Capability for Asymmetric Supercapacitors

Shi Jin Zhu[a], Jia Qi Jia[a], Tian Wang[a], Dong Zhao[a], Jian Yang[a], Fan Dong[b]*, Zheng Guo Shang[c], Yu Xin Zhang[a,c]*

Two kinds of novel CeO_2@MnO_2 nanostructures have been synthesized via a self-assembly strategy. The as-prepared CeO_2 nanowire@MnO_2 nanostructures exhibited unprecedented pseudocapacitance performance (255 F g^{-1}) with outstanding rate capability. A new mechanism based on the synergistic effect between CeO_2 and MnO_2 was proposed to interpret this phenomenon. When assembled as an asymmetric supercapacitor, an energy density of 27.5 Wh kg^{-1} with a maximum power density of 1.6 kW kg^{-1} was achieved for CeO_2 nanowire@MnO_2 nanostructures.

Supercapacitors, also called electrochemical capacitor (EC), have been deemed to be the most promising devices for energy storage for their high power density and long cyclic life.[1-3] Manganese dioxide (MnO_2) has been supposed to the most talented transition metal oxides for pseudocapacitors after ruthenium dioxide (RuO_2) because of their high theoretical capacity (1370 F g^{-1}), large potential window (-0.2-1.0 V), non-toxicity and long cycling life.[4,5] To be sure, the electrochemical performances of supercapacitor depend largely on the active component. Thus, a large number of MnO_2 based nanocomposites have been designed to enlarge the active site or enhance the electrical conductivity of the nanocomposites for supercapacitors, including Co_3O_4@MnO_2, TiO_2@MnO_2, $NiCo_2O_4$@MnO_2 and SiO_2@MnO_2.[6-9] Unfortunately, they all suffer from the low gravimetric capacitance for the poor electrochemical performance of substrate in neutral electrolyte and helpless to the capacity of MnO_2 resulting in a low energy density when assembled a device. Thus, functional metal oxides coupled with MnO_2 should contribute to the capacity of the nanocomposites and help to reflect the capacitance of MnO_2.

As a member of rare earth element, cerium has received a great attention for its unique chemical properties. The specific electronic orbit brings an enhanced catalytic performance for CeO_2 when coupled with MnO_2.[10,11] The high activity of CeO_2 makes it easy to be oxidized and restored during the oxidation-reduction process.[12] A synergistic mechanism of oxidation-reduction was proposed for CeO_2@MnO_2 as a catalys.[13] In other words, CeO_2 is helpful to the reflecting of catalytic performance of MnO_2. Recently, a series of pure CeO_2 and CeO_2-based nanocomposites is used as supercapacitor electrode materials.[14,15] However, the low theoretical capacity and messy electrical conductivity of CeO_2 lead to a poor electrochemical property.[16,17] For this reason, CeO_2 is always considered to be a useless electrode material with few eyes on it in energy storage area. However, the high chemical activity of CeO_2 was considered to be an important property of electrode materials. To our knowledge, CeO_2@MnO_2 nanocomposites for supercapacitors have never been reported.

Here, we developed a facile strategy to design and fabricate the first CeO_2@MnO_2 composites for high-performance supercapacitors, where uniform CeO_2 octahedrons or nanowires acted as the matrix and δ-MnO_2 nanosheets were grown on the surface of the matrix. The CeO_2@MnO_2 composites as electrode materials demonstrated multiple advantages as follows: 1) The MnO_2 nanosheets were well-grown and well-dispersed on surface of CeO_2 nanostructures, significantly enhancing the effective utilization of active materials. 2) the independent CeO_2 nanostructures wrapped by ultrathin MnO_2 nanosheets formed abundant pores, which would enable a fast, reversible Faradaic reaction, and provide a short ion diffusion path during charge–discharge process; 3) the CeO_2 cores acted as an accelerator which could enhance the degree of Faradaic reaction between MnO_2 and electrolyte during the electrochemical test. More significantly, we found that the CeO_2 nanowire@MnO_2 nanostructures exhibited unprecedented high capacitance (255 F g^{-1}) with outstanding rate capability in three-electrode system. Remarkably, when the CeO_2 nanowire@MnO_2 nanostructure was applied in a real device, a specific capacitance of 49.5 F g^{-1} and energy density of 27.5 Wh kg^{-1} with a maximum power density of 16.0 kW kg^{-1} were achieved in 1 M Na_2SO_4 electrolyte.

The CeO_2@MnO_2 composite was synthesized by a two-step solution route (See the details in ESI). Fig. 1 shows the XRD patterns of pure CeO_2 and CeO_2@MnO_2 nanostructures. As clearly shown in Fig. 1a, all the peaks are indexed to CeO_2 (JCPDS 43-1002) indicating the high purity of the substrate. The peaks are sharp with high intensity manifesting the splendid crystallinity and low defect in CeO_2 octahedron. After coupling with MnO_2 nanosheets, the intensity of CeO_2 octahedron is not influenced, making the broad peaks pointing to δ-MnO_2 nanosheets (JCPDS 80-1098) too hard to be distinguished. In contrast to CeO_2 octahedron, the peaks of CeO_2 nanowires are incisive but its intensity is relatively low. When coupled with MnO_2, obvious peaks indicating δ-MnO_2 nanosheets appear in the composites. The otherness in XRD patterns between the two nanostructures can be ascribed to the different degree of crystallinity and content of MnO_2. The weight content of MnO_2 is calculated to be 21.6% and 41% for CeO_2 octahedron@MnO_2 nanostructures and CeO_2 nanowire@MnO_2 nanostructures respectively by treating these nanostrucures in 1 M HCl solution.

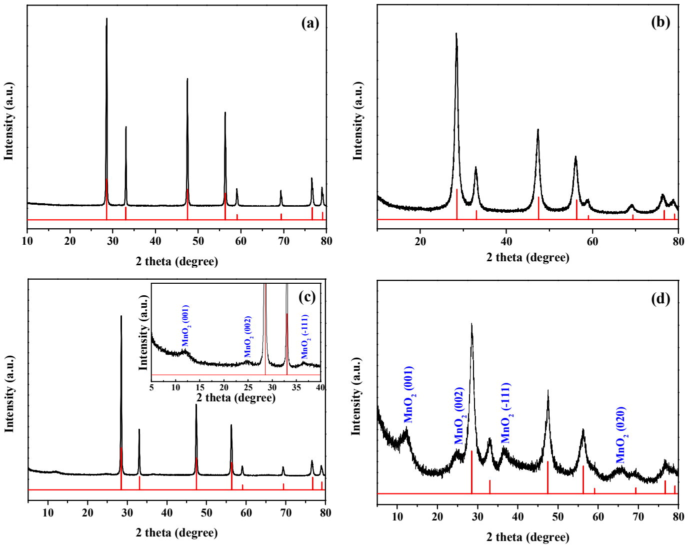

Fig .1 XRD patterns of (a) CeO_2 octahedron; (b) CeO_2 nanowire; (c) CeO_2 octahedron@MnO_2 nanostructure; (d) CeO_2 nanowire@MnO_2 nanostructure.

The detailed structural information of the composites was further investigated by TEM (Fig. 2). As displayed in Fig. 2a, several "box-like" structures are gathered together with each of them wrapped with thousands of nanosheets indicating the successful modification of MnO_2. The morphology of these boxes can be confirmed to be octahedron from SEM images (Fig. S1). Besides, the sizes of the CeO_2 octahedron@MnO_2 nanostructures are ranged from 200-400 nm with the shells thickness of 40 nm (Fig. 2b). Fig. 2c shows two distinct lattice spacings of ~0.69 nm and ~0.19 nm (inset of Fig. 2c), which correspond to the (001) plane of δ-MnO_2 and (220) plane of CeO_2. However, when replacing the CeO_2 octahedron with CeO_2 nanowires as the substrate, a great many of δ-MnO_2 nanosheets are pasted on the surfaces of ultrathin CeO_2 nanowires with a uniform shapes (Fig. 2d). The diameter of ultrathin CeO_2 nanowires can be calculated to be ~ 9 nm with the MnO_2 shells of ~20 nm (Fig 2e). The MnO_2 nanosheet can be affirmed of the ultrathin nature from the low distinguishability in TEM images. The interplanar spacings of 0.31 and 0.24 nm are corresponded to the (111) plane of CeO_2 and (-111) planes of δ-MnO_2 (Fig 2f). The homogeneous structure of these samples proves the synthetic strategy can be used to prepare uniform electrode materials. These findings demonstrate that the surface of CeO_2 can be modified with interconnecting MnO_2 nanosheets, which enlarge the contact area between electrolytes leading to an enhanced electrochemical property.

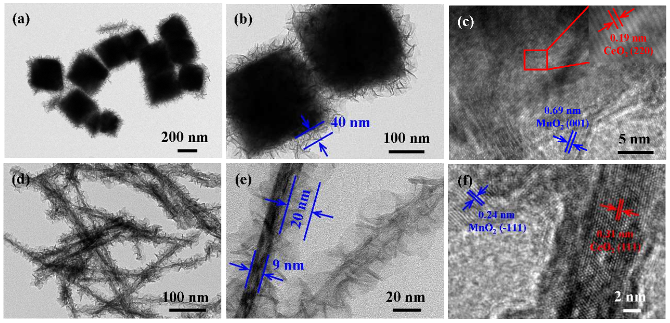

Fig .2 TEM images of (a-c) CeO_2 octahedron@MnO_2 nanostructure; (d-f) CeO_2 nanowire@MnO_2 nanostructure.

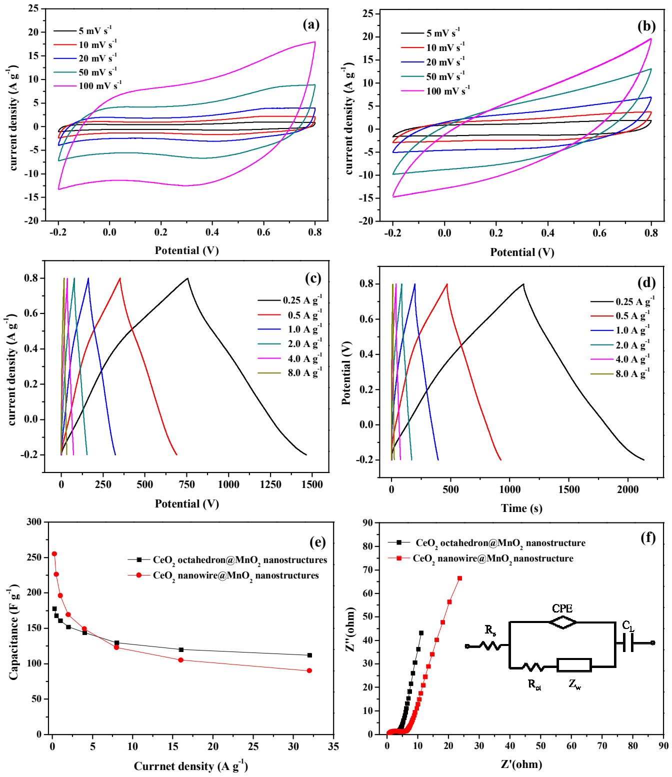

Fig. 3 The electrochemical performance of the two kinds of nanostructures: Cyclic voltammograms of (a) CeO_2 octahedron@MnO_2 nanostructure and (b) CeO_2 nanowire@MnO_2 nanostructure; galvanostatic charge-discharge curves of (c) CeO_2 octahedron@MnO_2 nanostructure and (d) CeO_2 nanowire@MnO_2 nanostructure; (e) specific capacitance of the two kinds of nanostructures measured under different current densities; (f) Nyquist plots of the two kinds of nanostructures with inset showing the corresponding equivalent circuit.

The electrochemical properties of these two nanostructures were evaluated in a three-electrode system. As shown in Fig. 3a, the nearly rectangular CV curves at different scan rates of CeO_2 octahedron@MnO_2 nanostructures indicate the efficient charge transfer and the nearly ideal capacitive behaviors.[18] This can be ascribed to the rational content of MnO_2 and internal CeO_2 octahedrons which enhances the electrochemical performance of the MnO_2 nanosheets. However, the CV curves of CeO_2 nanowire@MnO_2 nanostructures almost change to shuttle-like shapes indicating the relatively poor rate capability (Fig. 3b). This can be imputed to the high content of MnO_2 in CeO_2 nanowire@MnO_2 nanostructures resulting in a relatively inefficient transfer of the charges. Nevertheless, the linear voltage−time profile and highly symmetric charge/discharge characteristics are indicative of good capacitive behavior achieved by these two novel structures (Fig. 3c and 3d). The specific capacitance of CeO_2 octahedron@MnO_2 nanostructures and CeO_2 nanowire@MnO_2 nanostructures are calculated to be 178.5 F g^{-1} and 255.2 F g^{-1} at the current density of 0.25 A g^{-1}, according to eqn: $Cs = I\Delta t/(m\Delta V)$. The favourable capacitance can certainly be attributed to the internal CeO_2 which enhances the electrochemical performance of the MnO_2 nanosheets. Fig. 3e shows the specific capacitances of CeO_2@MnO_2 nanocomposites with different MnO_2 contents recorded at different current densities. Actually, due to the reduced surface area accessed by the electrolyte at a high current density, the curves show a slight decrease with the increase of current density. Nevertheless, the specific capacitance of CeO_2 octahedron@MnO_2 nanostructures remains as high as 62.9 % of its initial capacity at a current density of 32.0 A g^{-1} (Fig 3e), which is higher than that of the similar nanostructure combined metal oxides with MnO_2 reported before.[19,20] The outstanding rate capability of CeO_2 octahedron@MnO_2 nanostructures can be attributed to the synergy effect. By contrast, the rate capability of CeO_2 nanowire@MnO_2 nanostructure is relatively poor even though the capacitance is higher than that of CeO_2 octahedron@MnO_2 nanostructures. This may be caused by the high content of MnO_2 which obtain a high capacitance at low current density but attenuate greatly in high current density resulting in an unconspicuous acceleration by CeO_2 nanowire. In detail, the MnO_2 reveals their capacity sufficiently at a low current density, the capacitance are rest with the MnO_2 content in the nanocomposites, which can be attributed to the adequately reaction between active materials and electrolyte. When the current density was raised to high-level, the MnO_2 could not emerge their capacity fully due to the low reaction depth. The high content of CeO_2 of CeO_2 octahedron@MnO_2 nanostructures ensures the acceleration compared to CeO_2 nanowire@MnO_2 nanostructure which makes the capacitance of CeO_2 octahedron@MnO_2 nanostructures higher than that of CeO_2 nanowire@MnO_2 nanostructure. Thus, a synergy effect based on CeO_2 and MnO_2 is proposed. During the electrochemical test, the CeO_2 cores act as an accelerator. In the process of oxidation, the CeO_2 and MnO_2 release their electron at the same time due to the mandatory potential difference. However, the high activity of CeO_2 makes it easy to be oxidized and restored during the oxidation-reduction process. Thus, CeO_2 despoils the electrons from MnO_2 uninterrupted which enhances the degree of the oxidation of MnO_2 resulting in an enhanced electrochemical performance and vice versa. These plunder process occurs along the electrochemical test and accomplishes quickly. Thus, no redox peaks can be found in CV curves. These findings provide a new electrochemical mechanism to explain the interaction between two heterogeneous components.

The Nyquist plots were measured to analyze the otherness of these two nanostructures (Fig. 3f). The Nyquist plots exhibit a nearly semicircle over the high frequency range, followed by linear part in the low frequency region, which illustrate typical capacitor behavior. By contrast, the Ohm resistances (Rs) of CeO_2 nanowire@MnO_2 nanostructure corresponding to the resistance of electrolyte and the internal resistance of the active materials are almost the same as that of CeO_2 octahedron@MnO_2 nanostructures (0.53 Ω vs 0.55 Ω). However, the interfacial Faradic charge transfer resistance (Rct) of CeO_2 nanowire@MnO_2 nanostructure is almost three times of that of CeO_2 octahedron@MnO_2 nanostructures. The difference in Rct can be used to explain the otherness of these two nanostructures in rate capability. Thus, the CeO_2@MnO_2 nanostructures are supposed to be an excellent electrode material with high capacity, outstanding rate capability

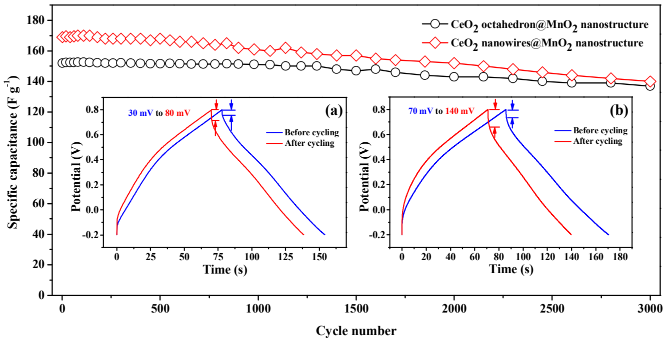

Fig .4 Variations of capacitance with cycle numbers for the two kinds of nanostructures at the current density of 2.0 A g^{-1}. Insets show the galvanostatic charge-discharge curves of (a) CeO_2 octahedron@MnO_2 nanostructures and (b) CeO_2 nanowire@MnO_2 nanostructures.

The cycle stability of as-prepared nanostructures was measured at a scan rate of 2.0 A g^{-1} for up to 3000 cycles. The specific capacitance of the two samples was decreased against to the cycling number. After 3000 cycles, the CeO_2 octahedron@MnO_2 nanostructure discharge capacities still retained 137 F g^{-1} with 90.1% of the initial available specific capacitance remained. By contrast, the CeO_2 mamowire@MnO_2 nanostructure remained 82.8% of the specific capacitance. The good cycle stability can be attributed to the persistent acceleration of CeO_2. Thus, the CeO_2@MnO_2 nanostructures are supposed to be an excellent electrode material to prepare high performance supercapacitors.

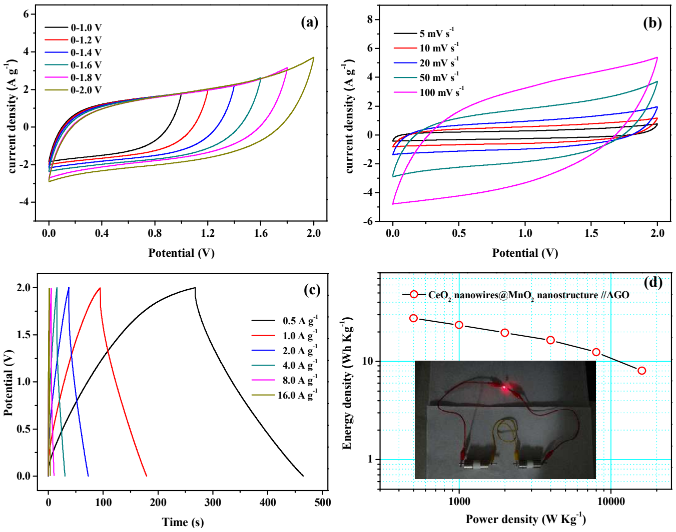

Fig. 5 Capacitive performances of an asymmetric supercapacitor with CeO_2 nanowire@MnO_2 nanostructure as positive electrode and active graphene oxide (AGO) as negative electrode: (a) CV curves at different cell voltages a scan rate of 50 mV s^{-1}; (b) CV curves recorded at different scan rates with a maximum cell voltage of 2.0 V; (c) Galvanostatic charge-discharge curves at different current densities between 0 and 2.0 V. (d) Ragone plots of the asymmetric supercapacitor. The inset shows the digital image of a red-light-emitting diode (LED) lighted by the as-prepared device

To further explore the electrochemical performance of the nanostructure in real system, an asymmetric supercapacitor was fabricated using the CeO_2 nanowire@MnO_2 nanostructure as the positive electrode and the activated graphene oxide (AGO) as the negative electrode with 1.0 M Na_2SO_4 aqueous electrolyte. The mass ratio of negative electrode and positive electrode were 2.46 mg cm^{-2} and 2.21 mg cm^{-2}, respectively based on charge balance theory.[21] Fig. 5a exhibits the CV curves of the asymmetric supercapacitor cell with voltages varying from 0-1 V to 0-2 V. The asymmetric supercapacitor exhibits an ideal capacitive behavior with nearly rectangular CV curves even at potential window up to 2.0 V. Moreover, the rectangular CV shape can still be well preserved at a maximum cell voltage of 2.0 V at scan rate as high as 100 mV s^{-1}, indicating a good rate capability of the asymmetric supercapacitor (Fig. 5b). The capacitance of the asymmetric supercapacitor is calculated to be 49.5 F g^{-1} based on the total weight of the electrodes at a current density of 0.25 A g^{-1} (Fig. 5c). The supercapacitor delivers an energy density of 27.5 Wh kg^{-1} with a maximal power density of 1.6 KW kg^{-1} for a 2.0 V window voltage. These values are much higher than those of the symmetrical supercapacitors and MnO_2-based asymmetric supercapacitors.[22,23] Such an excellent capacitive performance can be ascribed to the high chemical activity of CeO_2 nanowires@MnO_2 nanocomposite and the synergetic role of the two asymmetric electrodes. Thus, we connected our capacitors to a red LED and successfully lighted it (inset of Fig. 5d). More importantly, the LED was on for over 10 minutes after charged for 30 seconds at 2.0 V.

Conclusions

In summary, we have developed a facile self-assembly strategy to construct CeO_2@MnO_2 nanostructure with outstanding rate capability for supercapacitors owning to the synergistic effect between CeO_2 and MnO_2. An asymmetric supercapacitor based on the CeO_2 nanowire@MnO_2 nanostructure as the positive electrode and AGO as the negative electrode delivers an energy density of 27.5 Wh kg^{-1} at a power density of 500 W kg^{-1}. These findings point out a new direction in developing high performance supercapacitors for practical applications.

The authors gratefully acknowledge the financial supports provided by National Natural Science Foundation of China (Grant no. 51104194), International S&T Cooperation Projects of Chongqing (CSTC2013gjhz90001), National Key laboratory of Fundamental Science of Micro/Nano-device and System Technology (2013MS06, Chongqing University), State Education Ministry and Fundamental Research Funds for the Central Universities (Project no. CDJZR14135501 and 106112015CDJXY120002, Chongqing University, PR China).

Notes and references

[a] College of Material Science and Engineering, Chongqing University, Chongqing, 400044, P.R. China.
[b] Chongqing Key Laboratory of Catalysis and Functional Organic Molecules, College of Environmental and Biological Engineering, Chongqing Technology and Business University, Chongqing 400067, P.R. China
[c] National Key Laboratory of Fundamental Science of Micro/Nano-Devices and System Technology, Chongqing University, Chongqing 400044, P.R. China
[*] E-mail: zhangyuxin@cqu.edu.cn; dfctbu@126.com;

† Electronic Supplementary Information (ESI) available. See DOI：10.1039/c000000x/

1 P. Simon, Y. Gogotsi, *Nat. Mater.*, 2008, **7**, 845.
2 J.R. Miller, P. Simon, **Science**, 2008, **321**, 651.
3 A.S. Aricò, P. Bruce, B. Scrosati, J.M. Tarascon, W. Van Schalkwijk, *Nat. Mater.*, 2005, **4**, 366-377.
4 J. Liu, J. Jiang, M. Bosman, H.J. Fan, *J. Mater. Chem.*, 2012, **22,** 2419.
5 W. Xiao, J.S. Chen, X.W. Lou, *CrystEngComm*, 2011, **13**, 5685.
6 J. Liu, J. Jiang, C. Cheng, H. Li, J. Zhang, H. Gong, H.J. Fan, *Adv. Mater.*, 2011, **23**, 2076.
7 X. Lu, M. Yu, G. Wang, T. Zhai, S. Xie, Y. Ling, Y. Tong, Y. Li, *Adv. Mater.*, 2013, **25**, 267.
8 L. Yu, G. Zhang, C. Yuan, X.W. Lou, *Chem. Commun.,* 2013, **49**, 137.
9 C. Xu, F. Kang, B. Li, H. Du, *J. Mater. Res.*, 2010, **25**, 1421.
10 G. Qi, R.T. Yang, *J. Phys. Chem. B*, **108**, 2004, 15738.
11 Z.Y. Ding, L. Li, D. Wade, E.F. Gloyna, *Ind. Eng. Chem. Res.*, 1998, **37**, 1707.
12 S. Tang, J. Lin, K. Tan, *Catal. Lett.*, 1998, **51**, 169.
13 Z.Q. Zou, M. Meng, Y.Q. Zha, *J. Phys. Chem. C*, 2009, **114**, 468.
14 Y. Wang, C.X. Guo, J. Liu, T. Chen, H. Yang, C.M. Li, *Dalton Trans.*, 2011, **40**, 6388.
15 N. Padmanathan, S. Selladurai, *RSC Adv.*, 2014, **4**, 6527.
16 E. Lavik, I. Kosacki, H. Tuller, Y. Chiang, J. Ying, *J. Electroceram.*, 1997, **1**, 7.
17 H. Tuller, A. Nowick, *J. Electrochem. Soc.*, 1979, **126**, 209.
18 M. Zhi, C. Xiang, J. Li, M. Li, N. Wu, *Nanoscale*, 2013, **5**, 72.
19 W. Li, G. Li, J. Sun, R. Zou, K. Xu, Y. Sun, Z. Chen, J. Yang, J. Hu, *Nanoscale*, 2013, **5**, 2901.
20 Z.Q. Zhang, C.C. Ma, M. Huang, F. Li, S.J. Zhu, C. Hua, L. Yu, H.L. Zheng, X.B Hu, Y.X. Zhang, *J. Mater. Scie.*, 2015, **1**,.
21 Z. Fan, J. Yan, T. Wei, L. Zhi, G. Ning, T. Li, F. Wei, *Adv. Funct. Mater.*, 2011, **21**, 2366.
22 L. Deng, G. Zhu, J. Wang, L. Kang, Z. H. Liu, Z. Yang, Z. Wang, *J. Power Sources*, 2011, **196**, 10782.
23 Q. Cheng, J. Tang, J. Ma, H. Zhang, N. Shinya, L.C. Qin, *Carbon*, 2011, **49**, 2917.